ISSN 0915-633X

NATIONAL INSTITUTE FOR FUSION SCIENCE

The Origins of Elctrical Resistivity in Magnetic Reconnection:
Studies by 2D and 3D Macro Particle Simulations

M. Tanaka

(Received - Mar. 14, 2001)

NIFS-688 Apr. 2001

RESEARCH REPORT
NIFS Series

TOKI, JAPAN

The Origins of Electrical Resistivity in Magnetic Reconnection: Studies by 2D and 3D Macro Particle Simulations

Motohiko Tanaka
Research and Information Center, National Institute for Fusion Science
Toki 509-5292, Japan (Email: mtanaka@nifs.ac.jp)

This article argues the roles of electrical resistivity in magnetic reconnection, and also presents recent 3D particle simulations of coalescing magnetized flux bundles. Anomalous resistivity of the lower-hybrid-drift (LHD) instability, and collisionless effects of electron inertia and/or off-diagonal terms of electron pressure tensor are thought to break the frozen-in state that prohibits magnetic reconnection. Studies show that, while well-known stabilization of the LHD instability in high-beta plasma condition makes anomalous resistivity less likely, the electron inertia and/or the off-diagonal electron pressure tensor terms make adequate contributions to break the frozen-in state, depending on strength of the toroidal magnetic field. Large time-and-space scale particle simulations show that reconnection in magnetized plasmas proceeds by means of electron inertia effect, and that electron acceleration results instead of Joule heating of the MHD picture. Ion inertia contributes positively to reconnection, but ion finite Larmor radius effect does negatively because of charge separation of ions and magnetized electrons. The collisionless processes of the 2D and 3D simulations are similar in essence, and support the mediative role of electron inertia in magnetic reconnection of magnetized plasmas.

Keywords: Electron inertia, off-diagonal terms of pressure tensor, collisionless plasma, no Joule heating
To appear in: Journal of Earth, Planets and Space, Japan (2001).

1. Roles of Resistivity in Magnetic Reconnection

From the beginning of magnetic reconnection studies in the middle of the 20th century, people recognized that merging of different magnetic field lines is possible if finite electrical resistivity is present on the MHD (magnetohydrodynamic) description[1]. However, the origins of such resistivity remained a mystery, since magnetic reconnection occurs typically in a few (poloidal) Alfven times τ_A which is by orders of magnitude less than the time τ_{col} of classical binary collisions,

$$\tau_A \ll \tau_{col}. \tag{1}$$

In the solar wind and magnetospheric environments, the classical collision time amounts to a few days, while magnetic reconnection breaks up in a few tens of minutes as observed by satellites.

The following *gedanken experiment* illustrates the role of electrical resistivity in the MHD picture. Two filaments that carry the same directional current, J_1 and J_2 in Fig.1, attract each other. The magnetic field is enhanced in time between the filaments. This induces the solenoidal electric field E_t via Faraday's law, $-c\nabla \times \mathbf{E} = \partial \mathbf{B}/\partial t$. If the filaments with radius r_0 are placed in vacuum as shown in Fig.1(a), there is nothing to stop the process; the filaments should merge in a time $(\sqrt{\pi}/2)\tau_A$, where $\tau_A = r_0/V_A$ and the Alfven speed $V_A = B_p/\sqrt{4\pi\rho_0}$ is defined using the rod mass density ρ_0 and the poloidal magnetic field B_p on their surface (Eq.(16) of Ref.12). In a plasma of Fig.1(b), by contrast, the electric field E_t inevitably accelerates the plasma electrons, forming the axial current J_3 at the separatrix. It must be noted that this current increases in time with its direction opposite to that of the approaching filaments. The repulsive forces acting between J_1 and J_3 and between J_2 and J_3 exceed the attractive force between J_1 and J_2, which blocks magnetic reconnection. However, if some mechanism exists limiting the growth of the induced current J_3, then the attractive force between the filaments J_1 and J_2 can overcome the repulsive ones, and magnetic reconnection proceeds. In other words, if electrical resistivity is sufficiently large for a given electric field E_t,

$$E_t = \eta J_3, \tag{2}$$

the *anti-reconnection* current $J_3 = E_t/\eta$ is kept small. Thus, the Ohm's law (2) is interpreted as the law to yield finite (non-infinite) solenoidal current at the separatrix via enhanced resistivity η. But, it must be emphasized that the Ohm's law $E_t = \eta J$ of the MHD picture is an over-simplification, which does not adequately represent the collisionless process that is hidden behind the global reconnection process. For example, Joule heating is replaced by electron acceleration for the collisionless reconnection in magnetized plasmas, and by accelerated meandering electrons and ions for reconnection in the plasma sheet configuration.

For nearly half a century, people sought for the origins of electrical resistivity in a *collisionless plasma*[2–8,11–20]. Electron inertia resistivity[2] was first proposed as early as 1970, and was later applied to magnetically confined plasmas where strong magnetic field produces magnetic islands of their thickness roughly about the electron inertia length[3]. Meanwhile, anomalous resistivity was extensively studied without apparent success. In 1990's, particle simulations by different groups showed that electron inertia[12,13,20] and/or off-diagonal terms of electron pressure tensor[14,16–18] make adequate *collisionless* contributions to break the frozen-in state of magnetized plasmas

and the Harris-type equilibrium with a magnetic null at the X-point, respectively.

It might be an irony of history that anomalous resistivity became very popular in the research community of magnetic reconnection in early 1970's. Changes of magnetic topologies and heating of plasmas were argued in terms of various micro instabilities and their nonlinear consequences[4,5]. The electron inertia resistivity was almost forgotten for twenty years until it was re-spotlighted to explain the sawtooth oscillations of a tokamak core plasma[3], as mentioned above.

Anomalous resistivity is defined as the one that appears as nonlinear effects of wave-particle interactions[4], in analogy to electron scattering by phonons in solid-state physics. Waves can be generated by either electron or ion beams, or pressure gradients. However, such waves must be excited under the conditions of, say, the magnetosphere in which the plasma drift speed is rather small, $v_d \sim v_{th,i}$ (ion thermal speed), and the electron and ion temperatures are comparable, $T_e \sim T_i$. Many instabilities including those of ion acoustic and ion cyclotron waves were eliminated under these conditions, except for the lower-hybrid-drift (LHD) instability[5]. It is an electron drift wave that becomes unstable in resonance with unmagnetized ions. Its frequency range $\omega \leq \Omega_{LH}$ (lower-hybrid frequency) and persistence in the $T_e \sim T_i$ condition favored the LHD instability. Quasi-linear theory[5] and particle simulations[6,7] confirmed generation of anomalous resistivity if the waves were present.

Nevertheless, the LHD instability had a weakness, i.e. stabilization under high-beta conditions including magnetic null points. Data analysis of the GEOTAIL satellite shows that the LHD waves are present in the periphery of the plasma sheet but not at its center, and that their observed intensity is about an order of magnitude low in order to account for magnetic reconnection[8].

The electron inertia and/or the off-diagonal terms of electron pressure tensor break the frozen-in state of plasmas. They appear in the electric field equation as

$$\mathbf{E} = -\mathbf{v_e} \times \mathbf{B}/c - \nabla \cdot P_e/en - (m_e/e)(\mathbf{v_e} \cdot \nabla)\mathbf{v_e}. \quad (3)$$

By comparing magnitudes of the second and third terms in the right-hand side of Eq.(3), we can guess which of the terms is dominant in collisionless magnetic reconnection:

$$R_c \equiv (\nabla \cdot P_e/en)/((m_e/e)(\mathbf{v_e} \cdot \nabla)\mathbf{v_e}) \cong (L_e/L_p)(v_{te}/v_{\parallel e})^2, \quad (4)$$

where L_e and L_p are the scale lengths of the parallel bulk velocity and pressure of electrons, respectively, v_{te} the electron thermal speed, and $v_{\parallel e}$ the electron parallel drift acquired by acceleration during the X-point transit. We note the relation $v_{te}/V_A = (\beta_e m_i/m_e)^{1/2}(B_t/B_p)$, where $\beta_e = 8\pi n T_e/B^2$ is electron beta value with n and T_e electron density and temperature, respectively, and B_p and B_t the poloidal and toroidal magnetic field, respectively (B_p corresponds to the reconnecting magnetic field). In the magnetospheric plasma, the relations $v_{\parallel e} \sim V_A \ll v_{te}$ and $L_e < L_p$ lead to $R_c > 1$. This corresponds to a series of particle simulations by Hesse and his colleagues. On the other hand, in magnetically confined plasmas, one has $v_{\parallel e} \sim V_A \sim v_{te}$ and $L_e \ll L_p$. Therefore, one gets $R_c < 1$; electron inertia effect dominates over that of the pressure tensor term. These relations were confirmed by the macro-particle simulations for plasmas with a guide magnetic field[12,13].

The role of electron pressure and its numerical verifications are nicely described in Ref.14. The effect of electron inertia is very simple: the electrons that are the principal current carrier get accelerated and stream out of the so-called *diffusion region* (reconnection region) while holding the acquired current J_t. Hence, the current at the separatrix does not grow infinitely but remains finite. On equation, the separatrix current J_t is expressed in terms of the reconnection (solenoidal) electric field E_t,

$$J_t \cong J^{(e)} \sim (ne^2/m_e)E_t\tau_{tr}, \quad (5)$$

where e and m_e are the electronic charge and mass, respectively, and τ_{tr} is the electron transit time across the diffusion region. Simply rewriting the above equation yields the proportionality relation that has the form of *the Ohm's law,*

$$E_t = \eta_{ei} J_t, \ \eta_{ei} = m_e/e^2 n\tau_{tr}. \quad (6)$$

As remarked previously, released magnetic energy is converted to directed energy of accelerated electrons, and not to Joule heating. This is clearly seen in the shifted distribution function of electrons (cf. Fig.7 of Ref.12). This tells us the limitation of electrical resistivity which is an MHD-based concept.

Finally, collisionless reconnection was numerically investigated by several authors[11-20]. Even newly emerged particle simulation tools that can handle large space-and-time scale kinetics[9-11], including the *macro particle code* (Sec.2), were applied to magnetic reconnection of magnetized flux bundles. It showed that electron dynamics along the magnetic field limits the separatrix current and causes magnetic reconnection[11-13]. As a counter-proof, when the parallel electron motion (displacement) was numerically discarded, as is treated in the MHD theory (simulation), the separatrix current was tremendously enhanced, which prohibited magnetic reconnection. Thus, the electron inertia effect is proven to break the frozen-in condition and make reconnection possible in magnetized plasmas.

2. Large Time-and-Space Scale Simulations

It is sometimes advantageous to deal with electron and ion dynamics while leaving out small-scale, high-frequency wave activities. In standard electromagnetic

particle simulations, the grid size is taken at the Debye length, which numerically tends to mix up the phenomena of very different scales - small scale electrostatic phenomena and large scale magnetic phenomena; it may lead us to wrong findings that hardly occur in nature.

The macro-particle code HIDEN[9] and its counterpart in Los Alamos CELESTE[10] were designed to deal with large time-and-space scale plasma phenomena, in which the grid size Δx is typically the order of electron skin depth, and the time step Δt is chosen much larger than the plasma period,

$$\Delta x \gg \lambda_{De},\ \Delta t \gg \omega_{pe}^{-1}. \tag{7}$$

Here, λ_{De} is the Debye length and ω_{pe} is electron plasma frequency. Noisy plasma oscillations at $\omega \sim \omega_{pe}$ are eliminated from the simulations by the choice of a large time step, $\omega_{pe}\Delta t \gg 1$. To realize large time-and-space scale simulations, a slightly backward time-decentering technique is introduced[9-11]. The Maxwell equations with time level suffices are written as

$$\frac{1}{c}\left(\frac{\partial \mathbf{E}}{\partial t}\right)^{n+1/2} = \nabla \times \mathbf{B}^{n+\alpha} - \frac{4\pi}{c}\mathbf{J}^{n+\alpha}, \tag{8}$$

$$\frac{1}{c}\left(\frac{\partial \mathbf{B}}{\partial t}\right)^{n+1/2} = -\nabla \times \mathbf{E}^{n+\alpha}, \tag{9}$$

$$\nabla \cdot \mathbf{E}^{n+1} = 4\pi\rho^{n+1}, \tag{10}$$

$$\nabla \cdot \mathbf{B}^{n+1} = 0, \tag{11}$$

where $\mathbf{E}$ and $\mathbf{B}$ are the electric and magnetic fields, respectively, and α is a decentering (implicitness) parameter. The current density $\mathbf{J}$ and the charge density ρ in the Maxwell equations are implicit quantities, which are not the simple sums of known particle quantities but are expressed in terms of both the present and *unknown* future electromagnetic fields. To describe the particle motions, either the Newton-Lorentz equations or the drift-kinetic equations are used. The former includes the full Larmor radius effects, which is suited to treat meandering particles around magnetic null points[11]. The latter deals with the drift motions that arise from averaging over Larmor radii, and is more economical in computation when a guide magnetic field is present[12,13]. The Newton-Lorentz equations of motion are written as

$$\left(\frac{d\mathbf{v}_j}{dt}\right)^{n+1/2} = \frac{e_j}{m_j}\left(\mathbf{E}^{n+\alpha}(\mathbf{x}_j) + \frac{\mathbf{v}_j^{n+1/2}}{c} \times \mathbf{B}^{n+\alpha}(\mathbf{x}_j)\right), \tag{12}$$

$$\left(\frac{d\mathbf{x}_j}{dt}\right)^{n+1/2} = \mathbf{v}_j^{n+1/2}, \tag{13}$$

where $\mathbf{x}_j$ and $\mathbf{v}_j$ are the position and velocity of the jth particle, respectively. The parameter α that appears in the above equations controls selective damping of high-frequency oscillations with the frequency $\omega\Delta t \gg 1$; it should be chosen in the range $\frac{1}{2} < \alpha \leq 1$. By combining Eq.(8)-(13), we obtain a closed set of implicit equations that determines the electromagnetic fields, the particle positions and velocities of the future time level. The algorithm and technique are best summarized in the latest literature[11].

3. Magnetic Reconnection by 2D Simulations

As a simple model of studying the collisionless process of magnetic reconnection, we adopt merging of two flux bundles that carry the same directional current[12,13]. This process is called coalescence and was previously investigated as a mechanism of generating high-energy electrons and X-ray emissions from the stellar nebula[19,20]. The coalescence starts without initial electric field or the X-point current, unlike so-called driven reconnection. For this reason, one can identify synchronized development of the current and electric field at the X-point relatively at ease. This provides a clear physics picture of collisionless reconnection.

The flux bundles are isolated and initially at rest. The magnetic field is a sum of the poloidal magnetic field $\mathbf{B}_p$ that forms a separatrix between the flux bundles and the constant applied field $B_t\hat{y}$. The initial electric field is null everywhere; the reconnection electric field is the y-component E_y, which is decoupled in the 2D simulations from the electrostatic component $\mathbf{E}_p = (E_x, 0, E_z)$ at the separatrix. This is advantageous to examine the growth of the reconnection electric field.

A charge-neutral plasma is initialized in the doubly-periodic Cartesian system. The ions located in the core of the flux bundles carry axial current to produce the poloidal magnetic field. The system size is $L_x = 400c/\omega_{pe}$ and $L_z = 300c/\omega_{pe}$ with 320 × 72 grids. The interval of the grids is uneven in the x direction, with $\Delta x \cong 0.55c/\omega_{pe}$ in the central region (denoted by a small square in Fig.2(b)) and $\Delta x \cong 1.6c/\omega_{pe}$ in the outer region; on the other hand, $\Delta z \cong 4.1c/\omega_{pe}$ everywhere (note $c/\omega_{pe} = 7 \sim 15\lambda_{De}$). The number of electrons and ions is 64 per cell for each species with the particle splitting technique to reduce discreteness noise. It is remarked that particle simulation has a reasonable resolution even with fewer grid points than MHD (fluid) simulations because the plasma current and charge are carried by Lagrangean particles (not by Eulerian grid quantities). The physical parameters are the mass ratio $m_i/m_e = 25 - 200$, the temperature ratio $T_i/T_e \cong 0.1 - 50$, and the strength of the applied field $\omega_{ce}/\omega_{pe} = 0 - 2$ where $\omega_{ce} = eB_t/m_e c$. The electron beta value is $\beta_e = 8\pi n T_e/B_t^2 = 0.04$. Electrons are well-magnetized (Larmor radius $\rho_e \sim 1c/\omega_{pe}$), and their drifts are properly treated; ions are weakly magnetized ($\rho_i \sim 10c/\omega_{pe}$). On the other hand, short-length waves with $k\rho_e,\ k\lambda_e > 1$ are not included here, where ρ_e is electron Larmor radius. Interactions with these waves may be neglected in the present large scale

dynamics, since the electron cyclotron waves are excited only when the perpendicular temperature is high, $T_{\perp e}/T_{\parallel e} > 1$ or the parallel drift is as large as thermal speed, $V_\parallel > v_{te}$.

The essence of the simulation results with an applied magnetic field is briefly described. Figure 2 is the time snapshots of the poloidal flux function[12] Ψ defined by $\mathbf{B}_p = \nabla \times (\Psi \hat{y})$, for the times $t/\tau_A = 0.75$, 1.9 and 2.5, where $\tau_A = \frac{1}{2} d/V_A$ with d the initial separation of the flux bundles, and V_A is the poloidal Alfven speed. The temperature for this run is $T_i/T_e = 1$, the applied field strength $\omega_{ce}/\omega_{pe} = 1$, and typical value of the poloidal magnetic field $B_p/B_t \sim 0.2$. The flux bundles with the same directional axial current attract each other by magnetic forces, and they get flatly squeezed at the contact surface as shown in Fig.2(b) before an active phase of magnetic reconnection sets in. The formation of an elongated (Y-shaped) current layer is the characteristic feature of the Sweet-Parker reconnection[21,22]. The thickness of the current layer is a few times that of electron skin depth, $L_B \sim 3c/\omega_{pe}$ (half thickness). The thickness increases with reduction of the applied magnetic field B_p/B_t, and does slightly with ion mass. Occurrence of magnetic reconnection is roughly identified by counting the isolated poloidal flux contained in the flux bundles. The number of the isolated Ψ-contours decreases between the panels (b) and (c).

The time histories of the toroidal current J_y and electric field E_y measured in a small region containing the separatrix $(\frac{1}{2}L_x, \frac{1}{2}L_x)$ are shown in logarithmic scales in Fig.3. In the early phase up to $t \cong 2\tau_A$, both the toroidal electric field and current increase exponentially at the same growth rate. The toroidal current is carried mostly by the electrons that have been accelerated by the electric field during their transit through the separatrix region. It is emphasized that these electrons reside in the region only for a finite time. The proportionality relation $E_y \propto J_y$ resembles *the Ohm's law,* although it has by no means been imposed in the particle simulations. In subsequent steady phase, the isolated poloidal flux $\Delta\Psi$ decreases linearly in time, as consistent with nearly constant strength of the electric field E_y. In the 2D simulations, the isolated magnetic flux decreases monotonically and almost completely.

The poloidal components of the ion and electron currents, the electric and magnetic fields in a small rectangular region denoted in Fig.2(b) are shown in Fig.4. Ions and electrons stream vertically into the diffusion region with the velocity $v_{in} \sim 0.3 v_A$, and flow out sideways with the (poloidal) Alfven speed, $v_{out} \sim V_A$ after having been accelerated. Interestingly, the divergence of the electron and ion currents are separately non-zero, i.e., $\nabla \cdot \mathbf{J}^{(s)} \neq 0$ $(s = e,\ i)$. The former divergence is due to parallel motion of electrons along the field lines, and the latter one by ion polarization drift[13] in order to satisfy $\nabla \cdot \mathbf{J} = 0$ for the total current. The plasma outflow is not narrowly channeled but spreads within dual fans originating at the X-point. The plasma density is slightly higher in the flux bundles to satisfy the pressure balance $P + B^2/8\pi = const$, and is nearly homogeneous outside except for the current layer. A quadrapole sub-structure develops within the layer (Fig.2 of Ref.13). These features are somewhat different from a simple model of the Sweet-Parker reconnection.

A specially-designed simulation below confirms that the electron parallel dynamics is a key element of collisionless magnetic reconnection in magnetized plasmas. The poloidal projection of the electron displacement due to their motions along the magnetic field $v_\parallel \mathbf{B}/|B|$ is discarded, while their current and perpendicular motions are treated in an ordinary fashion[13]. This situation is equivalent to the MHD theory (simulation). The time history of the isolated poloidal magnetic flux contained in the flux bundles is shown in Fig.5, with the solid and dashed lines for the standard and special runs, respectively. In clear contrast to the standard run, the poloidal flux for the special run does not decrease. The enlarged plot of the magnetic field in the poloidal plane of Fig.6 shows the formation of a stagnant plasmoid at the X-point. This is a direct consequence of slow removal of the electrons (current carrier) out of the separatrix region. The plasmoid current $J_y < 0$ blocks an incoming plasma that carries the opposite-sign current $J_y > 0$ by repulsive magnetic forces. These results lead us to conclude that the parallel dynamics (motion) of the electrons is the mechanism of breaking the frozen-in state in magnetic reconnection of magnetized plasmas.

The parameter dependence of the reconnection rate[13] is depicted in Fig.7. Figure 7(a) shows the dependence on the ion inertia (electron mass is fixed). The reconnection rate is a smoothly increasing function of ion mass, and is scaled as $(1/\Psi)d\Psi/dt \propto (m_i/m_e)^{1/6}$ for $m_i/m_e \geq 50$. For the collisionless reconnection mediated by off-diagonal electron pressure tensor term, the rate was shown to scale[14] $(1/\Psi)d\Psi/dt \propto (m_i/m_e)^{1/4}$. Both scalings show monotonic and slow dependence on the ion inertia. Further, we note that the typical reconnection time $[(1/\Psi)d\Psi/dt]^{-1} \sim 5\tau_A$ is shorter than the two-fluid simulations without compressibility and thermal effects[20]. A dependence on the applied toroidal magnetic field is also shown with square symbols for $m_i/m_e = 100$. The thickness of the current layer D and the ratio D/L increase as the applied magnetic field is reduced. The reconnection rate increases only by 20% when the applied field is nullified for the coalescence process of mild-profile current. In this case, the plasma in the current layer is compressed as $< n_s > \sim n_0(2+\epsilon)/(1+\epsilon)$, where $\epsilon = B_t/B_p$ and n_0 is average plasma density. A simplified model that balances the incoming and outgoing mass fluxes in a rectangular box (diffusion region) yields, $d\Psi/dt \sim V_A D/L \propto < n_s >^{1/2}$. This roughly agrees with the observed increase in the reconnection rate for $B_t \to 0$.

The dependence on the ion Larmor radius is shown in Fig.7(b) [ion inertia is fixed, $m_i/m_e = 100$]. The reconnection rate is reduced when the ion Larmor radius becomes comparable with the ion skin depth, $\rho_i \geq c/\omega_{pi}$. This dependence is scaled as, $d\Psi/dt \sim F[\rho_i/(c/\omega_{pi}) \times (m_i/m_e)^{(1-\nu)/2}]$ where $\nu \cong 2.7$ and the $F(x)$ profile is given by Fig.7(b). For the mass ratio $m_i/m_e = 1836$, we expect the ion Larmor radius effect to set in for $\rho_i/(c/\omega_{pi}) \geq 10$. The negative role of the ion finite Larmor radius effect is attributed to charge separation of magnetized electrons and unmagnetized ions, as $\rho_e < L_B < \rho_i$. Since incoming ions tend to reside outside of the current layer due to large Larmor radii, a charge separation results; the poloidal electric field pointing to the current layer was actually observed in the macro particle simulation. This electric field generates the current $J_y < 0$ via the $E \times B$ drift of *magnetized* electrons, while ions hardly respond to this small scale electric field. Thus, the X-point current is enhanced, which suppresses magnetic reconnection (see the discussion of Fig.1 for the relation between the X-point current and reconnection speed).

4. Magnetic Reconnection by 3D Simulations

The settings of the 3D simulations are the same as those of the 2D ones except for addition of the y coordinate[23]. The size along the y-direction is $L_y = 2000c/\omega_{pe}$, with the periodic boundary condition. The number of grids in the y-direction is 60; the grid size is $\Delta y \cong 33c/\omega_{pe}$. The number of electrons and ions is 16 per cell for each species, and the mass ratio is $m_i/m_e = 100$. In order to let magnetic reconnection occur at one point, the initial currents of the flux bundles are slightly curved toward the separatrix at $y = \frac{1}{2}L_y$, as illustrated in Fig.8. The separation of the flux bundles is $0.5L_x$ at $y = 0$ and $0.4L_x$ at $y = \frac{1}{2}L_y$. The separatrix is a line of the length $\Delta Y \cong \frac{1}{10}L_y$ going through the point $\frac{1}{2}(L_x, L_y, L_z)$. Like the 2D simulations, reconnection occurs spontaneously by attraction of the flux bundles; there is no initial and external electric field that drives reconnection.

First, it is remarked that, when the initial loading is made 2D-like (no y-dependence), then reconnection occurs in a 2D fashion even for the 3D simulation environments. Reconnection proceeds monotonically and simultaneously in all the poloidal cross sections. Transition of the reconnection features from the 3D to 2D ones occurs gradually as L_y decreases since rapidly moving electrons along the magnetic field (with the $E \times B$ drift) tend to homogenize the anisotropy. The bifurcation of 2D and 3D-type reconnections is considered to occur around the separatrix length $\Delta Y \sim \frac{1}{2}L_y$, since half the domain in the $y-$direction needs to be a source and the other half a sink of plasma flow.

For the results below, the 3D initial loading is adopted. Figure 9 shows the time histories of the electric field E_y, the toroidal current J_y, the difference of the vector potential A_y between the separatrix and the center of the flux bundle, and the distance between the flux bundles d_{p-p}, measured at $(y, z) = \frac{1}{2}(L_y, L_z)$ In the early time, plasma undergoes a self-adjustment stage toward an equilibrium. Then, the toroidal electric field and current repeat in-phase growth and decay, and the flux bundles bounce inward and outward in the 3D case. The amount of magnetic flux contained in the flux bundles decreases in a stepwise fashion. By contrast, in the 2D case of Fig.3, magnetic flux decreased monotonically without intermission. Also, the reconnection rate was sensitive to the electron thermal speed in the 2D case[13], but is found not so in the 3D case. These differences may be attributed to easiness of the current removal out of the separatrix for the 3D geometry, and partly to magnetic tension of curved magnetic field lines. In the 2D geometry, current-carrying electrons stream out of the separatrix region from a point to lines sideways, whereas in the 3D geometry the electrons spread out from a point to surfaces. The latter has more freedom of motion; magnetic reconnection may more directly reflect the global circumstances of the plasma.

Figure 10 shows the y-component of the vector potential A_y in consecutive six cross sections along the y-direction at four different phases, (a) equilibration at $t = 1.2\tau_{Ap}$, (b) first active phase at $t = 2.3\tau_{Ap}$, (c) pause at $t = 3.4\tau_{Ap}$, and (d) second active phase at $t = 4.5\tau_{Ap}$, where τ_{Ap} is the Alfven time defined by the poloidal magnetic field. For $t \geq 2.3\tau_{Ap}$, the contours are well squeezed at $y \sim \frac{1}{2}L_y$. An elongated current layer is well and steadily formed only at this position, and the current layer in other y locations varies in time. Thus, magnetic reconnection is sensitive to the plasma conditions. Apart from the central region to both the y-directions, antisymmetric helical deviation of the magnetic surfaces is seen in the poloidal cross-cuts. This asymmetry due to that of the toroidal electron current in the vicinity of the separatrix is characteristic of the 3D coalescence process with the applied magnetic field.

This asymmetry in 3D reconnection is better seen in the scalar potential φ ($\mathbf{E}_p = -\nabla\varphi$) of Fig.11, as in the same format as for Fig.10. The $\mathbf{E}_p$ field drives the plasma into and out of the separatrix through the $\mathbf{E} \times \mathbf{B}$ drift ($\mathbf{B} \cong B_t\hat{y}$). A quadrapole structure that carries plasma vertically inward toward the separatrix and ejects it sideways is formed only at the $y \cong \frac{1}{2}L_y$ cross section. The other quadrapole structure at the $y = 0$ cross section for $t = 2.3\tau_{Ap}$ is opposite in sign (dashed contours correspond to negative values), which pumps the plasma out of the separatrix; a closed circulation of the plasma flow is established in the toroidal plane.

Figure 12 shows the enlarged plot of the ion and electron currents J_i, J_e, and the electric and magnetic fields E, B in a small square region (see Fig.2(b)) at the central cross section $y = \frac{1}{2}L_y$ for the first active phase

$t = 2.3\tau_{Ap}$. The upper and lower panels correspond to the poloidal and toroidal components, respectively. We see dual ejection fans originating at the separatrix in the poloidal currents $\mathbf{J}_i$ and $\mathbf{J}_e$, and also the clearly formed current layer in the toroidal current $J_{e,y}$. The thickness of the current layer, the open angle of the ejection fans, and the ejection speed of the plasma ($V_{out} \cong V_A$) are quite the same as their 2D counterparts depicted in Fig.4 (plot formats of Figs.4 and 12 are identical). The poloidal motions of the ions and electrons deduced from J_i and J_e are consistent with the $E \times B$ drift calculated with the poloidal electric field of Fig.11. The formation of the Y-shaped elongated current layer is also seen in the poloidal magnetic field. Although the repetitive time histories of Fig.9 and insensitivity to the electron thermal speed showed 3D characteristics, the physics quantities at the separatrix (Fig.12) are much like their 2D counterparts.

Other interesting feature of the 3D reconnection is the oscillations of magnetic field on a long time scale, as depicted in Fig.13. The oscillation amplitude of magnetic energy B^2 increases when the coalescence process is almost finished. These oscillations have a period of $\cong 2\tau_{Ap}$, which is roughly equal to $\tau_{Ap}^{NL} = R^{NL}/V_{Ap}$ with R^{NL} the radius of merged flux bundles. This phenomenon that is observed for non-turbulent reconnection is mainly attributed to the toroidal component of the magnetic field, in which (electro)magnetic waves of $k_{\parallel} \neq 0$ are involved. This phenomenon will be analyzed and reported in near future.

5. Summary

It was argued in this article that the frozen-in state of a plasma that prohibits magnetic reconnection is broken either by electron inertia or the off-diagonal terms of pressure tensor depending on whether the plasma is magnetized or unmagnetized. Namely, in the former case the growth of the separatrix current that *suppresses* magnetic reconnection is limited by the escape of current-carrier electrons along the magnetic field. This is intrinsically a *non-MHD* effect, and is termed as *electron inertia resistivity*. However, this is not real dissipation, and collisionless reconnection leads to bulk acceleration of electrons along the magnetic field, instead of Joule heating. On the other hand, anomalous resistivity can still add to inertia resistivity although the lower-hybrid-drift instability was argued as less likely by theoretical and observational points of view.

The instantaneous features of the 3D collisionless reconnection at the separatrix were similar to those of the 2D reconnection. However, differences were insensitivity of the reconnection rate to the electron temperature (thermal speed), and more sensitivity to the plasma conditions in the 3D case. This reflects the easiness of the separatrix current removal, in which electrons escape from the X point to surfaces for the 3D geometry.

Acknowledgments

The author is grateful to his colleagues with whom he discussed collisionless magnetic reconnection and the origins of electrical resistivity, the studies of which were commenced as his Ph.D. dissertation of the lower-hybrid-drift instability and later arrived at the electron inertia effects with the use of his Macro-Particle code. The 3D numerical simulations were performed with the VPP300/16R supercomputer at the Astronomical Data Analysis Center of the National Astronomical Observatory, Japan.

References

1. J.W.Dungey, *Phys.Rev.Lett., 6,* 47 (1961).
2. T.W.Speicer, *Planet.Space Sci., 18,* 613 (1970).
3. J.A.Wesson, *Nucl. Fusion, 30,* 2545 (1990).
4. N.A.Krall and P.C.Liewer, *Phys.Rev.A, 4,* 2094 (1971).
5. R.C.Davidson and N.T.Gladd, *Phys.Fluids, 18,* 1327 (1975).
6. D.Winske, *Phys.Fluids, 24,* 1069 (1981).
7. M.Tanaka, *PhD Dissertation* (University of Tokyo, 1981);
M.Tanaka and T.Sato, *J.Geophys.Res., 86,* 5552 (1981).
8. I.Shinohara, *PhD Dissertation* (University of Tokyo, 1996).
9. M.Tanaka, *J.Comput.Phys., 79,* 209 (1988); ibid. 107, 124 (1993).
10. H.X.Vu and J.U.Brackbill, *Comput.Phys.Commun., 69,* 253 (1992).
11. M.Tanaka, *Comput. Phys. Commun., 87,* 117 (1995).
12. M.Tanaka, *Phys. Plasmas, 2,* 2920 (1995).
13. M.Tanaka, *Phys. Plasmas, 3,* 4010 (1996).
14. M.Kuznetsova, M.Hesse, and D.Winske, *J.Geophys.Res., 105,* 7601 (2000); M.Hesse, K.Schindler, J.Birn, and M.Kuznetsova, *Phys.Plasmas, 6,* , 1781 (1999).
15. M.Hoshino, *J.Geophys.Res., 92,* 7368 (1987).
16. J.Dreher, U.Arendt and K.Schindler, *J.Geophys.Res., 101,* 27375 (1996).
17. H.J.Cai, D.Q.Ding and L.C.Lee, *Phys.Plasmas, 4,* 509 (1997).
18. M.Hesse and D.Winske, *J.Geophys.Res., 103,* 26 (1998).
19. T.Tajima, F.Brunel, and J.Sakai, *Astrophys.J., 258,* L45 (1982).
20. D.Biskamp, E.Schwartz and J.F.Drake, *Phys.Rev.Lett., 75,* 3850 (1995).
21. A.Sweet, *Nuovo Cimento, 8,* 188 (1958).
22. E.N.Parker, *Astrophys.J.Suppl., 77,* 177 (1963).
23. M.Tanaka, *Magnetic Reconnection in Space and Laboratory Plasmas, Focused Talk* (The University of Tokyo Symposium, February 28 - March 4, 2000).

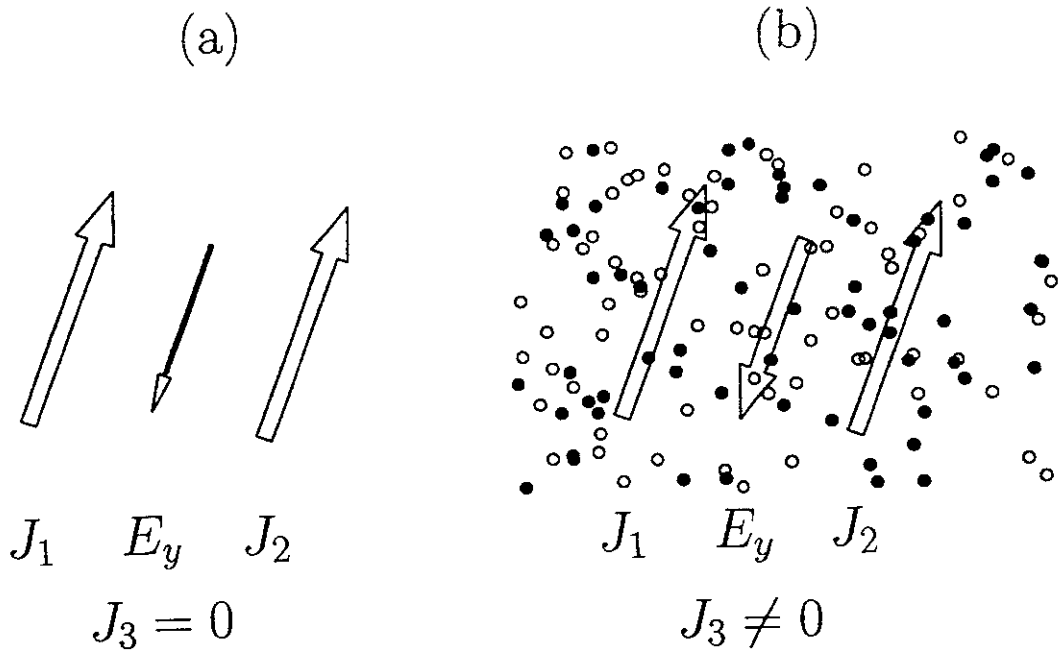

Figure 1. A gedanken experiment that illustrates the meaning of electrical resistivity for magnetic reconnection (a) in vacuum, and (b) in a plasma (dots represent plasma ions and electrons). The currents J_1 and J_2 flow in the flux bundles, while J_3 in the plasma does not exist initially and is induced by the electric field E_t during the reconnection process.

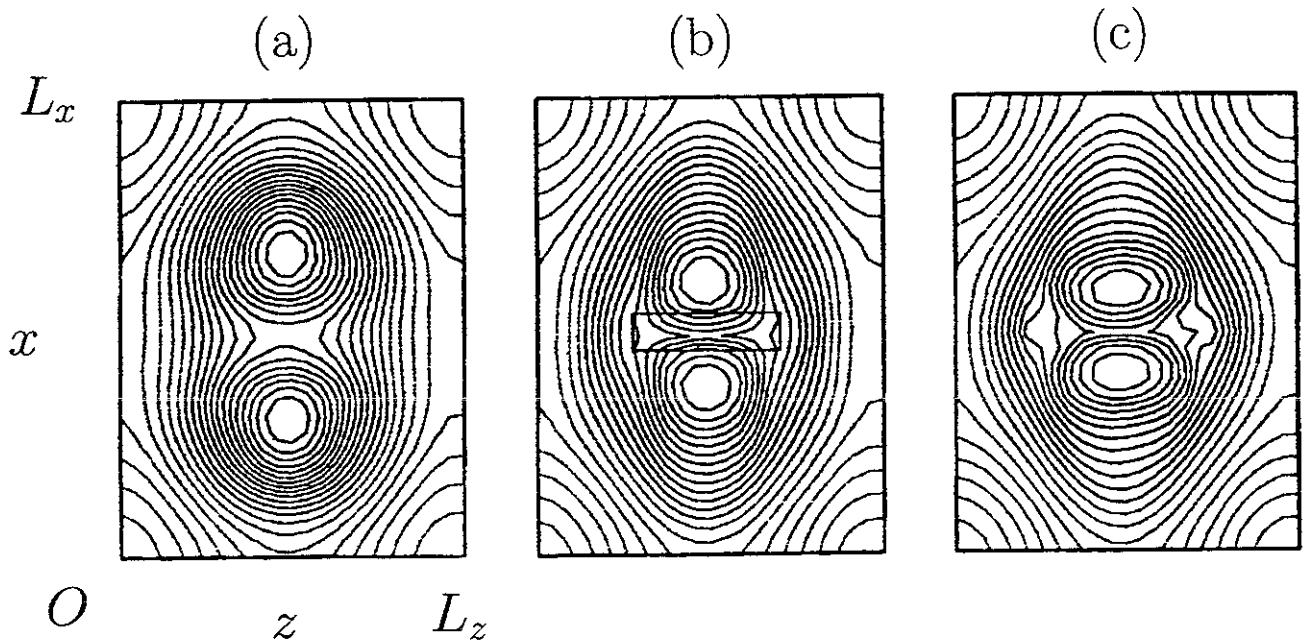

Figure 2. Snapshots of the poloidal flux function in (a) the equilibrium state $t = 0.75\tau_A$, (b) the most active phase of reconnection $t = 1.9\tau_A$, and (c) $t = 2.5\tau_A$.

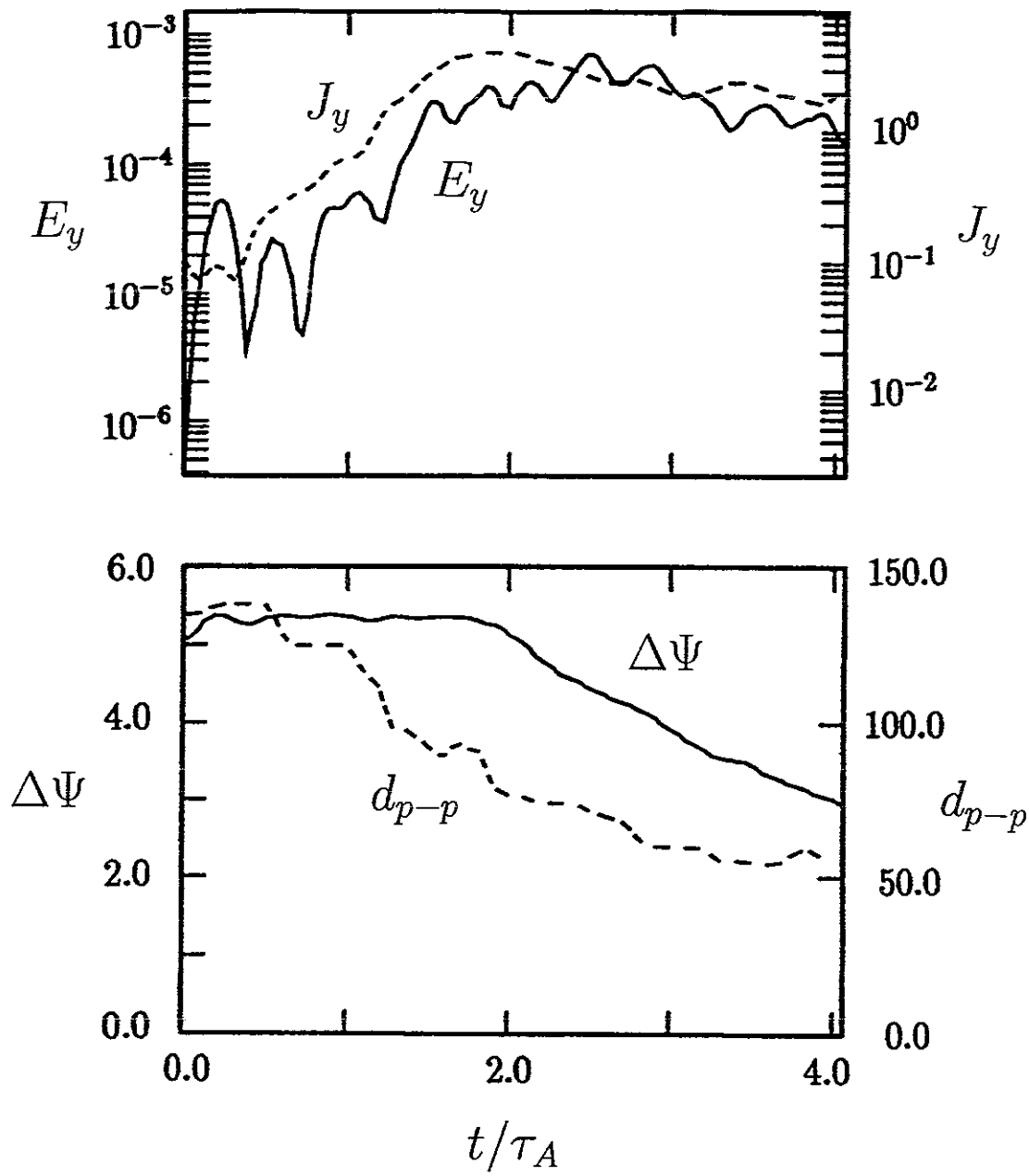

Figure 3. Time histories of the toroidal electric field E_y, and the toroidal current J_y in the upper panel, and those of the isolated poloidal flux $\Delta\Psi$ contained in the flux bundles, and the distance between the flux bundle centers d_{p-p} in the lower panel. These quantities except d_{p-p} are measured at the separatrix, and the signs of E_y and J_y are reversed.

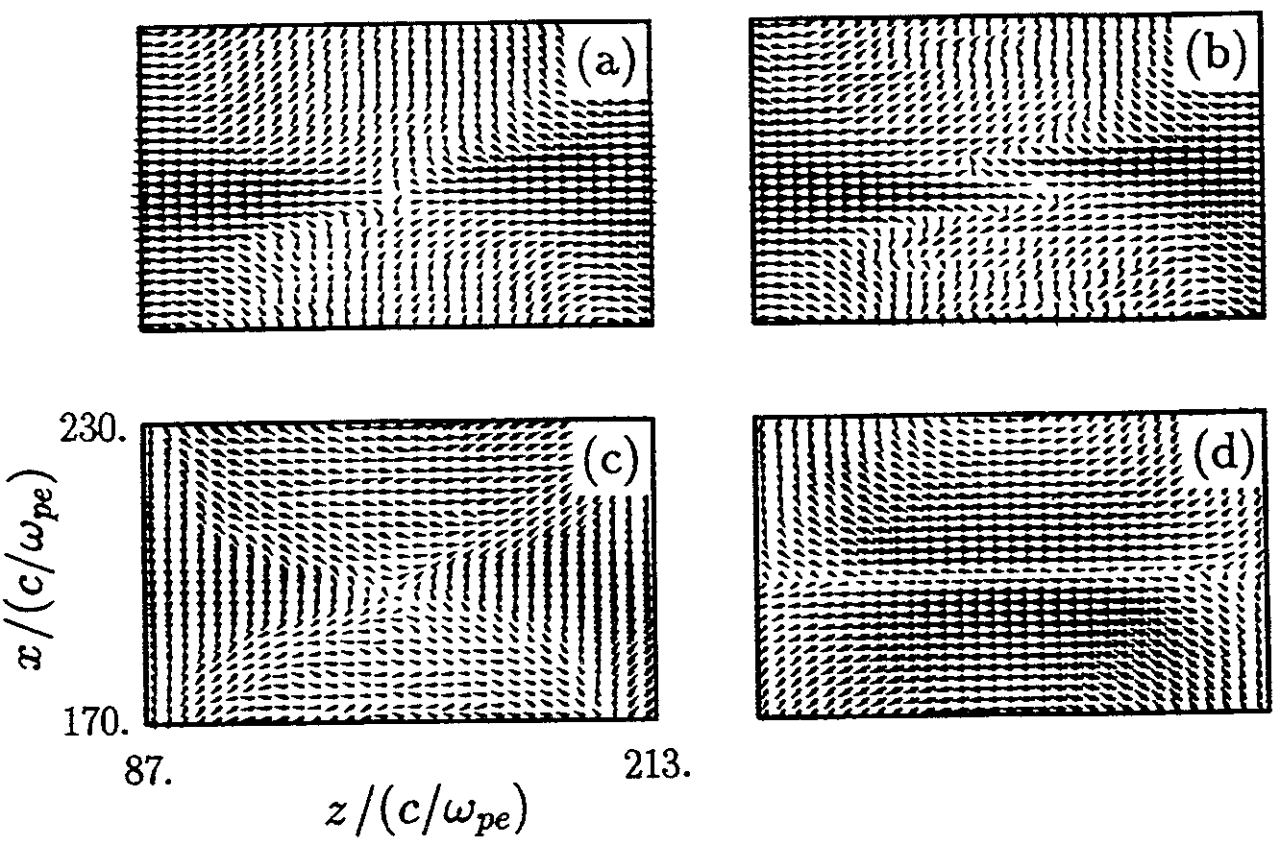

Figure 4. Enlarged plots of the poloidal quantities in the vicinity of the separatrix (in a small rectangular box of Fig.2(b)). The ion and electron currents in (a) and (b), respectively, and the electric and magnetic fields in (c) and (d).

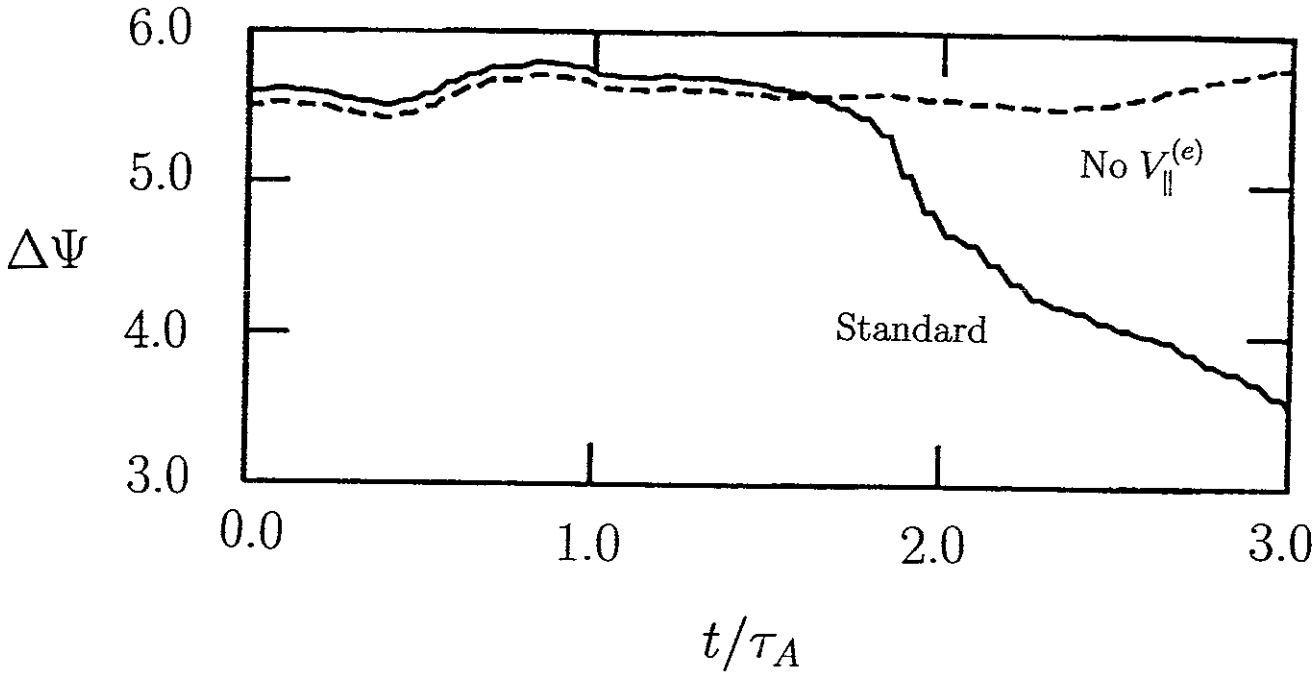

Figure 5. Time history of the isolated poloidal flux for the standard run (solid), and for the special run (dashed) in which spatial displacement of electrons along the magnetic field is discarded while keeping the toroidal current, i.e. the MHD case.

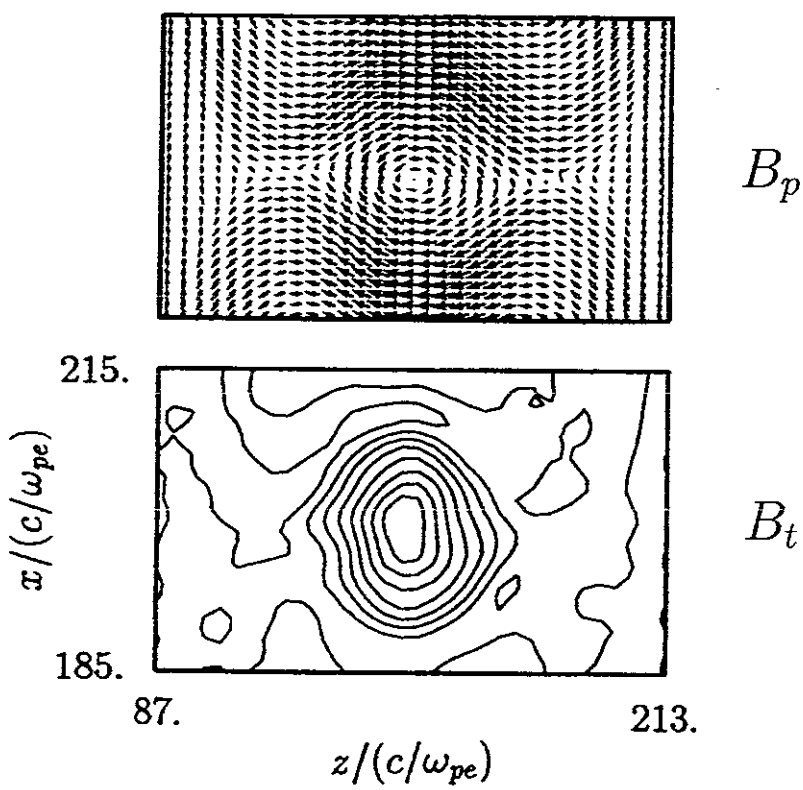

Figure 6. The poloidal and toroidal magnetic field for the special run in Fig.5 at $t = 3\tau_A$. The plasmoid stays at the separatrix and impedes magnetic reconnection.

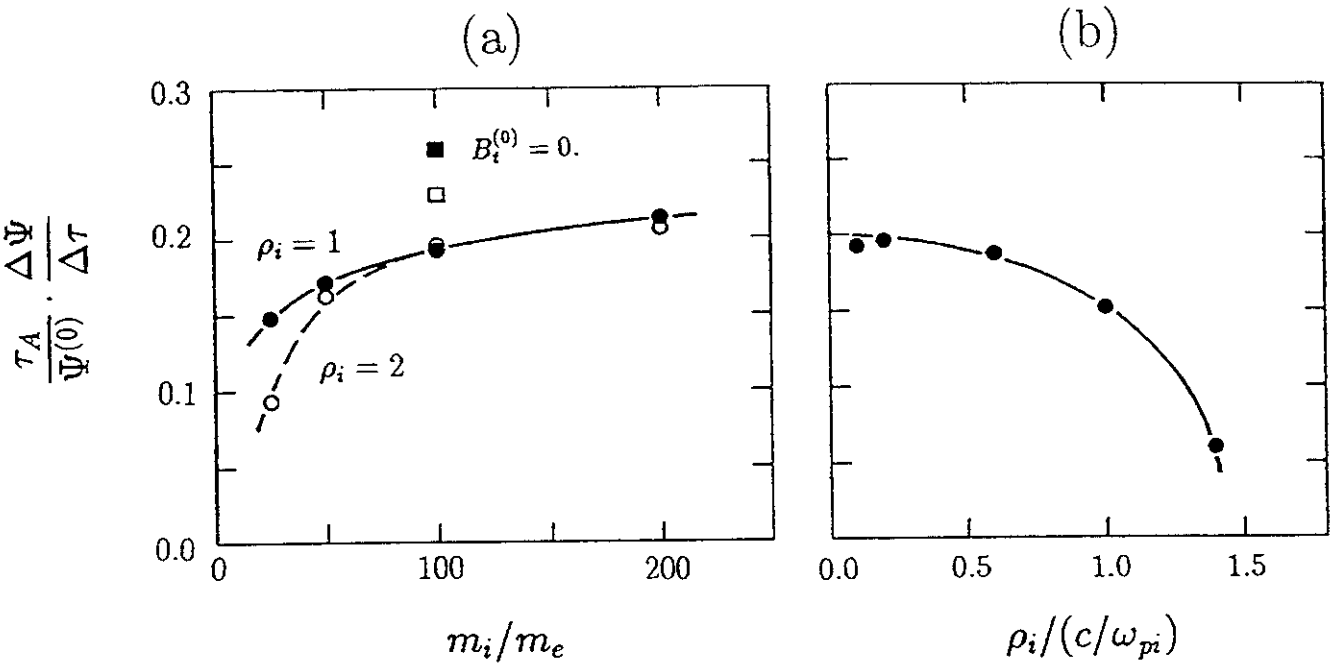

Figure 7. The parametric dependences of the reconnection rate on (a) the ion mass (for $\rho_i = 1$, $2c/\omega_{pe}$), and (b) the ion Larmor radius (for $m_i/m_e = 100$). Also in (a), the reconnection rates for the applied toroidal magnetic field of $B_t = 0$ and 0.2 are plotted with solid and open squares, respectively.

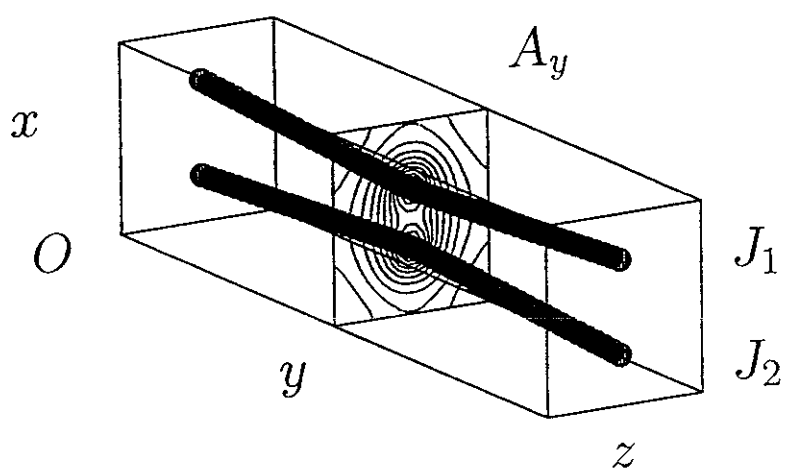

Figure 8. Schematic illustration of the geometry for the 3D simulation. The dots represent the axial current J_1 and J_2 carried by ions, and contours on the poloidal cross section show the y-component of the vector potential A_y.

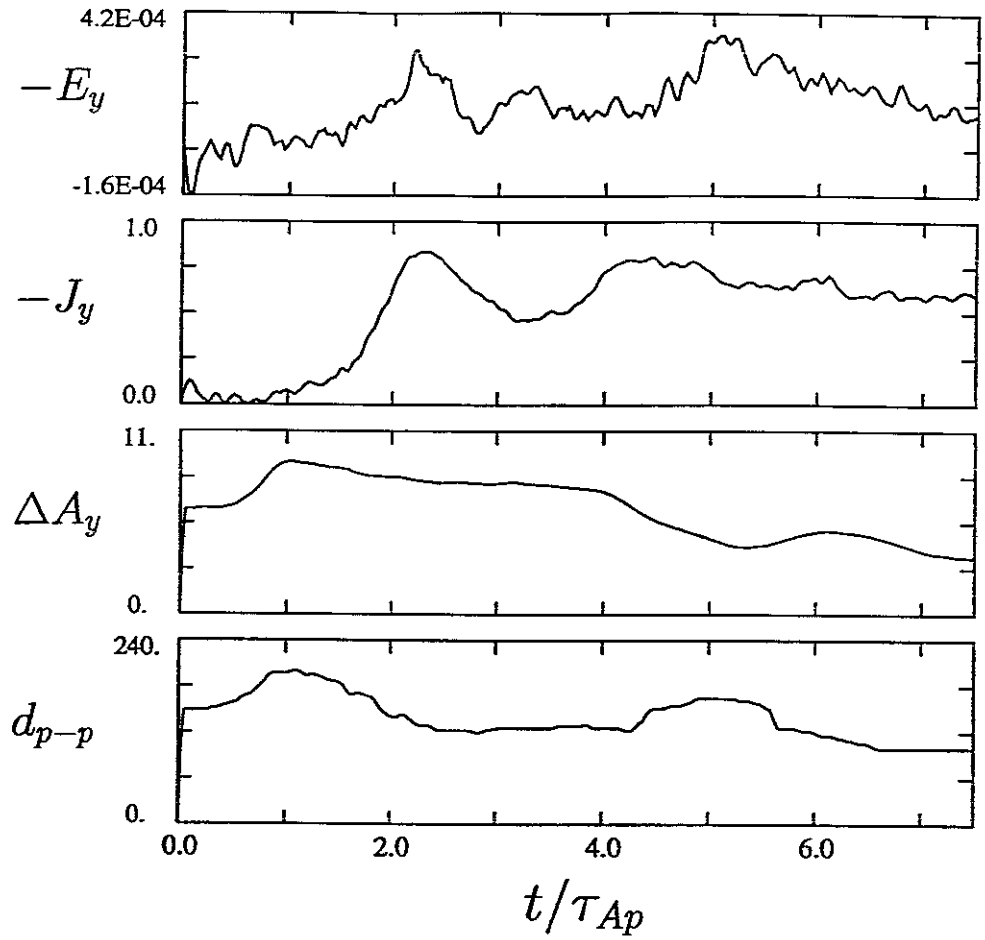

Figure 9. The time histories of the toroidal electric field E_y and current J_y, the difference of the vector potential between the separatrix and flux bundles ΔA_y, and the distance between the flux bundles d_{p-p} for the 3D reconnection.

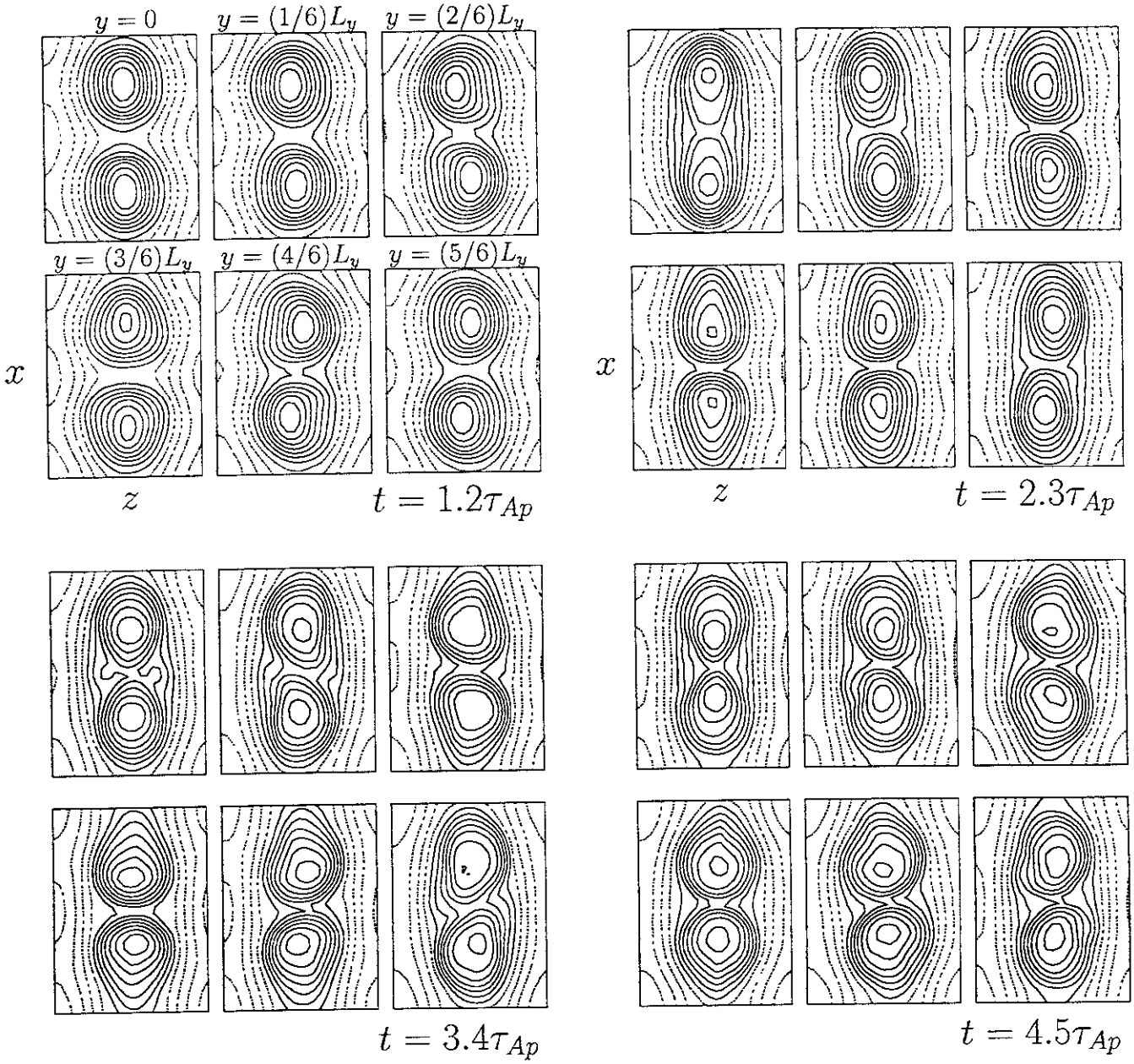

Figure 10. Snapshots of the y-component of the vector potential A_y at six cross sections along the y direction (the order is from left to right, then top to bottom), at four times $t/\tau_A = 1.2$, 2.3, 3.4 and 4.5.

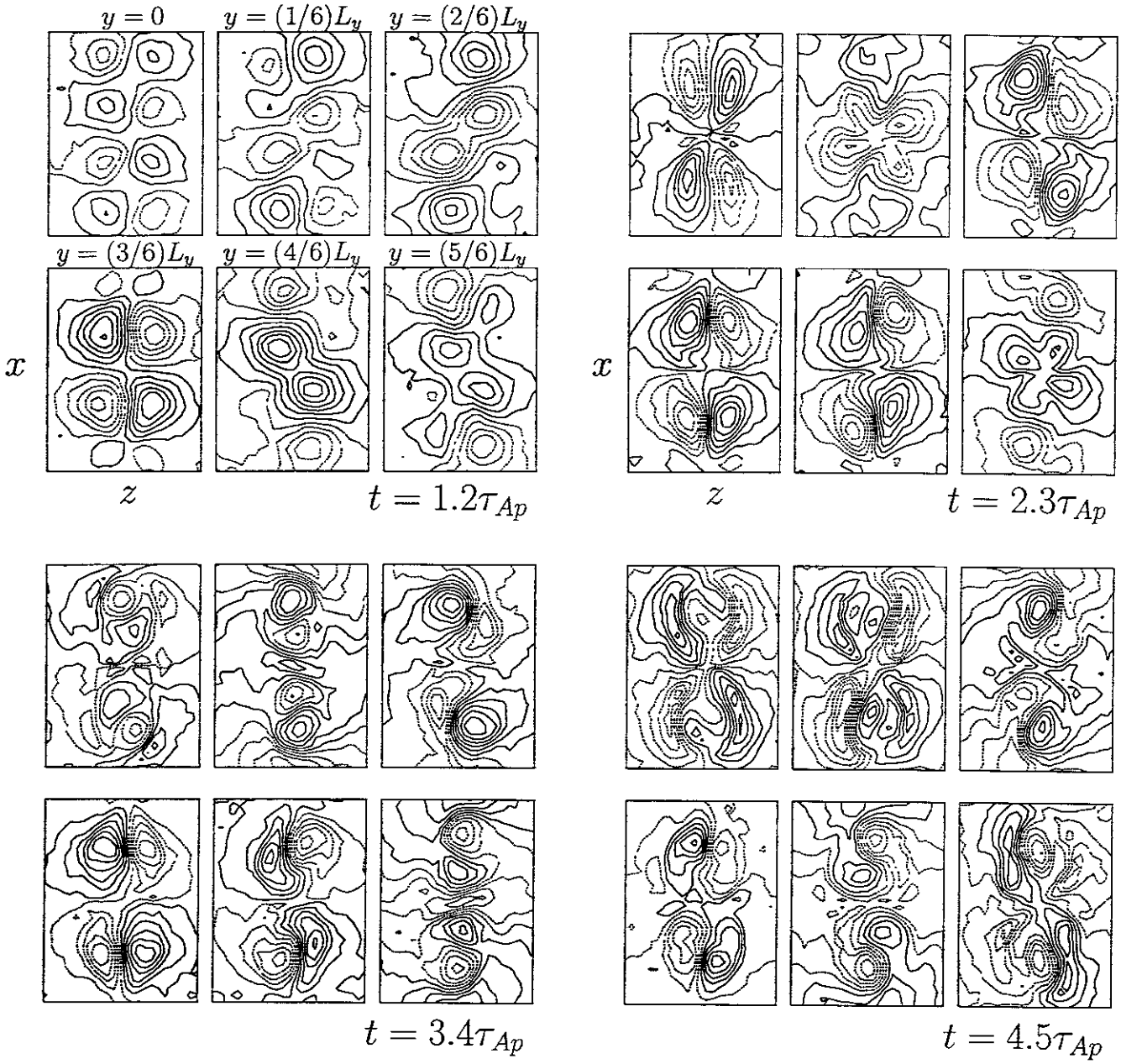

Figure 11. Snapshots of the scalar potential φ ($\mathbf{E}_p = -\nabla\varphi$) at six cross sections along the y direction (the order is from left to right, then top to bottom), at four times $t/\tau_A = 1.2$, 2.3, 3.4 and 4.5.

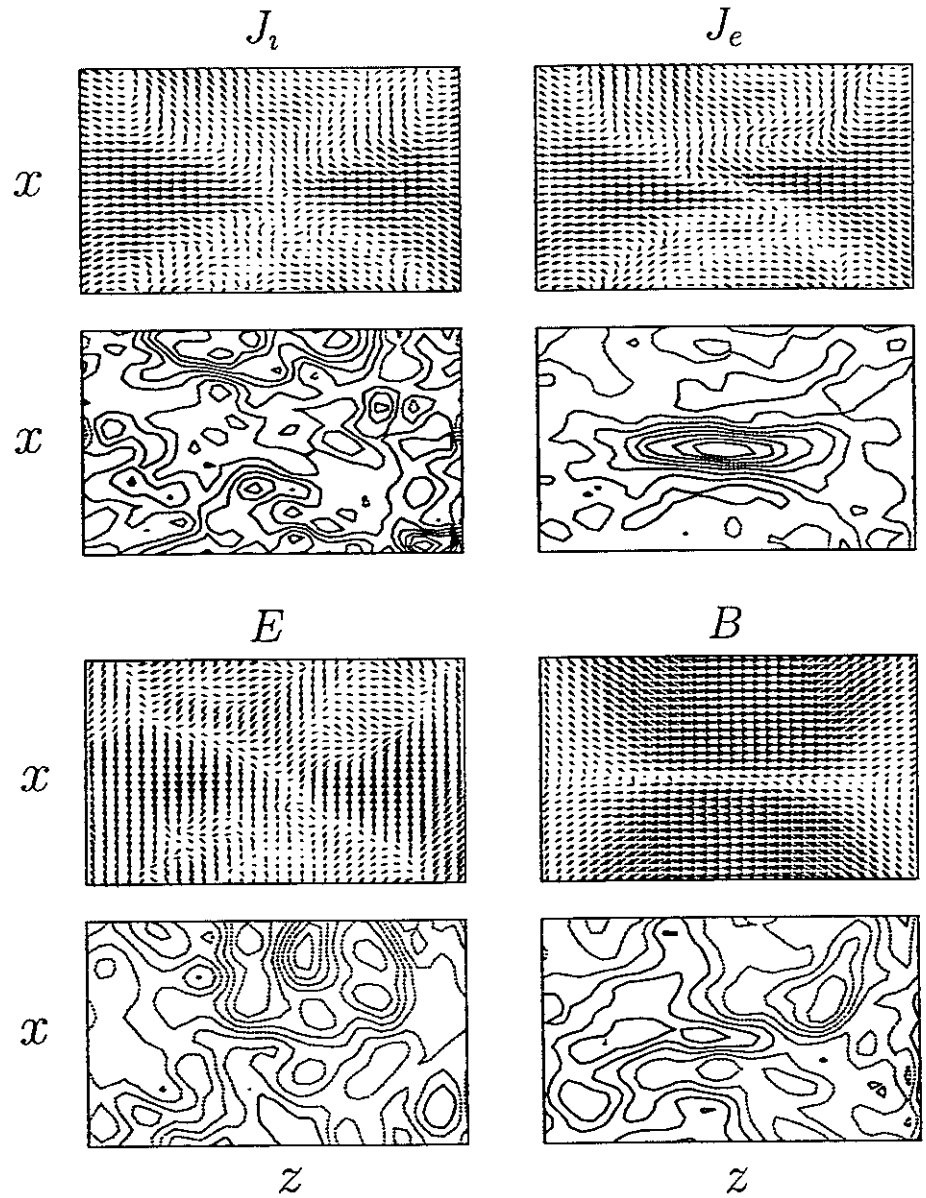

Figure 12. Enlarged plots of the poloidal quantities in the vicinity of the separatrix at $t = 2.3\tau_A$ of Fig.9 (plot format is the same as that of Fig.4). The ion and electron currents J_i and J_e in the top row, and the electric and magnetic fields E, B in the bottom row. In each group, the upper and lower panels correspond to the poloidal and toroidal components, respectively.

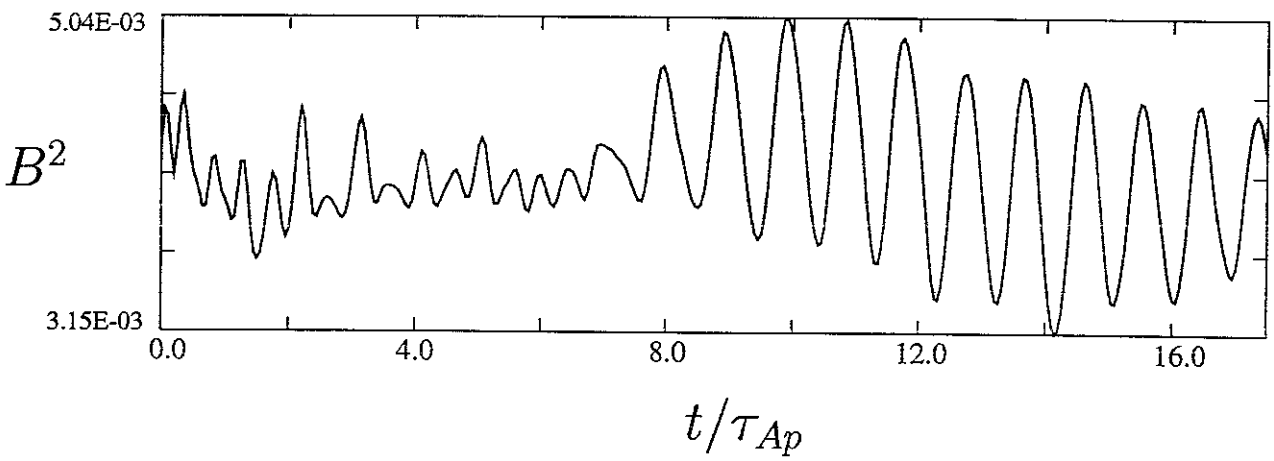

Figure 13. Oscillations in the magnetic energy B^2 on a long time scale, which are mainly due to the toroidal component of the magnetic field.

Recent Issues of NIFS Series

NIFS-664 N Nakajima
Three Dimensional Ideal MHD Stability Analysis in $L=2$ Heliotron Systems Oct 2000

NIFS 665 S Fujiwara and T Sato
Structure Formation of a Single Polymer Chain I Growth of trans Domains Nov 2000

NIFS 666 S Kida,
Vortical Structure of Turbulence Nov 2000

NIFS 667 H Nakamura, S Fujiwara and T Sato,
Rigidity of Orientationally Ordered Domains of Short Chain Molecules Nov 2000

NIFS-668 T Mutoh, R Kumazawa T Seki, K Saito, Y Torii F Shimpo G Nomura, T Watari D A Hartmann M Yokota K Akaishi, N Ashikawa, P deVries, M Emoto H Funaba, M Goto K Ida H Idei, K Ikeda, S Inagaki N Inoue, M Isobe O Kaneko, K Kawahata, A Komori T Kobuchi S Kubo S Masuzaki, T Morisaki, S Morita, J Miyazawa, S Murakami T Minami, S Muto, Y Nagayama, Y Nakamura H Nakanishi K Narihara, N Noda, K Nishimura K Ohkubo, N Ohyabu, S Ohdachi, Y Oka, M Osakabe, T Ozaki, B J Peterson, A Sagara N Sato, S Sakakibara, R Sakamoto, H Sasao, M Sasao, M Sato, T Shimozuma, M Shoji, S. Sudo, H Suzuki, Y Takeiri, K Tanaka, K Toi T Tokuzawa, K Tsumori, K Y Watanabe T Watanabe, H Yamada, I Yamada, S Yamaguchi, K Yamazaki, M Yokoyama, Y Yoshimura Y Hamada, O Motojima M Fujiwara
Fast- and Slow-Wave Heating of Ion Cyclotron Range of Frequencies in the Large Helical Device Nov 2000

NIFS-669 K Mima, M S Jovanovic, Y Sentoku Z-M Sheng, M M Skoric and T Sato
Stimulated Photon Cascade and Condensate in Relativistic Laser-plasma Interaction Nov. 2000

NIFS-670 L Hadzievski, M M Skoric and T Sato,
On Origin and Dynamics of the Discrete NLS Equation Nov 2000

NIFS-671 K Ohkubo, S Kubo, H Idei, T Shimozuma, Y Yoshimura F Leuterer M Sato and Y Takita,
Analysis of Oversized Sliding Waveguide by Mode Matching and Multi-Mode Network Theory Dec 2000

NIFS-672 C Das, S Kida and S Goto,
Overall Self-Similar Decay of Two-Dimensional Tirbulence Dec 2000

NIFS-673 L A Bureyeva, T Kato, V S Lisitsa and C Namba
Quasiclassical Representation of Autoionization Decay Rates in Parabolic Coordinates. Dec 2000

NIFS-674 L A Bureyeva, V.S Lisitsa and C Namba,
Radiative Cascade Due to Dielectronic Recombination Dec 2000

NIFS-675 M F Heyn, S V Kasilof, W. Kernbichler, K Matsuoka, V V Nemov, S Okamura, O S Pavlichenko,
Configurational Effects on Low Collision Plasma Confinement in CHS Heliotron/Torsatron, Jan 2001

NIFS-676 K Itoh,
A Prospect at 11th International Toki Conference - Plasma physics, quo vadis?, Jan 2001

NIFS-677 S Satake, H. Sugama, M Okamoto and M Wakatani,
Classification of Particle Orbits near the Magnetic Axis in a Tokamak by Using Constants of Motion, Jan 2001

NIFS-678 M Tanaka and A Yu Grosberg,
Giant Charge Inversion of a Macroion Due to Multivalent Counterions and Monovalent Coions Molecular Dynamics Studyn, Jan. 2001

NIFS-679 K Akaishi, M Nakasuga, H Suzuki, M Iima, N Suzuki, A Komori, O Motojima and Vacuum Engineering Group,
Simulation by a Diffusion Model for the Variation of Hydrogen Pressure with Time between Hydrogen Discharge Shots in LHD, Feb 2001

NIFS-680 A Yoshizawa, N Yokoi, S Nisizima, S -I Itoh and K Itoh
Variational Approach to a Turbulent Swirling Pipe Flow with the Aid of Helicity, Feb 2001

NIFS-681 Alexander.A.Shishkin
Estafette of Drift Resonances, Stochasticity and Control of Particle Motion in a Toroidal Magnetic Trap, Feb 2001

NIFS-682 H Momota and G H Miley,
Virtual Cathode in a Spherical Inertial Electrostatic Confinement Device, Feb 2001

NIFS-683 K Saito R Kumazawa T Mutoh, T Seki T Watari, Y Torii D A Hartmann Y Zhao, A Fukuyama, F Shimpo, G Nomura M Yokota, M Sasao M Isobe, M Osakabe, T Ozaki K Narihara, Y Nagayama, S Inagaki K Ida, S Morita, A V Krasilnikov K Ohkubo, M Sato, S Kubo, T Shimozuma, H Idei Y Yoshimura O Kaneko, Y Takeiri, Y Oka, K Tsumori K Ikeda A Komori H Yamada, H Funaba, K.Y Watanabe, S Sakakibara, M Shoji R Sakamoto, J Miyazawa, K Tanaka, B.J Peterson N Ashikawa S Murakami T Minami, S Ohakachi, S Yamamoto, S Kado, H Sasao, H Suzuki K Kawahata, P deVries M Emoto H Nakanishi T Kobuchi, N Inoue N Ohyabu Y Nakamura S Masuzaki S Muto K Sato T Morisaki M Yokoyama, T Watanabe M Goto I Yamada K Ida T Tokuzawa, , N Noda, S Yamaguchi K Akaish., A Sagara K Toi K Nishimura K Yamazaki, S Sudo Y Hamada, O Motojima, M Fujiwara
Ion and Electron Heating in ICRF Heating Experiments on LHD Mar 2001

NIFS-684 S Kida and S Goto,
Line Statistics Stretching Rate of Passive Lines in Turbulence Mar 2001

NIFS-685 R Tanaka, T Nakamura and T Yabe
Exactly Conservative Semi-Lagrangian Scheme (CIP CSL) in One Dimension Mar. 2001

NIFS-686 S Toda and K. Itoh,
Analysis of Structure and Transition of Radial Electric Field in Helical Systems Mar 2001

NIFS-687 T Kuroda and H Sugama,
Effects of Multiple-Helicity Fields on Ion Temperature Gradient Modes, Apr 2001

NIFS-688 M Tanaka,
The Origins of Elctrical Resistivity in Magnetic Reconnection Studies by 2D and 3D Macro Particle Simulations Apr 2001